Available online at www.sciencedirect.com
ScienceDirect
Trans. Nonferrous Met. Soc. China 35(2025) 3191−3202
Transactions of Nonferrous Metals Society of China
www.tnmsc.cn

Synergistic effect of Er and Si on corrosion resistance of peak-aged AlZnMgCu alloy

Shang-shang LIANG[1,2], Sheng-ping WEN[2], Ke-hong GUO[2], Bao-sheng LIU[1], Yong HU[1], Wu WEI[2], Xiao-lan WU[2], Hui HUANG[2], Kun-yuan GAO[2], Xiang-yuan XIONG[2], Zuo-ren NIE[2]

1. School of Materials Science and Engineering, Taiyuan University of Science and Technology, Taiyuan 030024, China;
2. School of Materials Science and Engineering, Beijing University of Technology, Beijing 100124, China

Received 9 February 2024; accepted 15 November 2024

Abstract: The corrosion resistance and mechanical properties of peak-aged AlZnMgCu alloys containing Si and Er elements were investigated with hardness test, tensile test, intergranular corrosion test, exfoliation corrosion test and transmission electron microscopy. The results indicate that peak-aged AlZnMgCuSiEr alloy is strengthened by co-precipitation of η' phases and nano-sized GPB-II zones. The yield strength of the AlZnMgCu alloy is increased by 38.5 MPa and the elongation is increased by 4.5%. At the same time, the corrosion resistance of the AlZnMgCuSiEr alloy is enhanced due to the synergistic effect of Er and Si. The maximum intergranular corrosion (IGC) depth decreases from 264.2 to 9.9 μm. The fundamental reason is that the co-addition of Si and Er regulates the evolution of precipitated phases in grains and at grain boundaries.

Key words: AlZnMgCu alloy; GPB-II zones; intergranular corrosion; exfoliation corrosion; mechanical properties

1 Introduction

Al−Zn−Mg−Cu alloys are extensively applied in the aerospace industry due to their excellent combined properties such as lightweight, superior strength, ductility, toughness, and fatigue resistance [1,2]. However, Al−Zn−Mg−Cu alloys exhibit susceptibility to corrosion cracking, so their applications are limited. Different forms of corrosion can occur in Al−Zn−Mg−Cu alloys due to damp air and industrial conditions, for example, exfoliation corrosion (EXCO), intergranular corrosion (IGC), and stress corrosion cracking (SCC) [3,4]. To further advance Al−Zn−Mg−Cu alloys, a crucial aspect is to enhance their corrosion resistance while simultaneously meeting the required mechanical properties.

Results in the literature [4,5] have shown that the simultaneous attainment of high strength and exceptional corrosion resistance in peak-aged Al−Zn−Mg−Cu alloys is an extraordinary challenge. High strength can be achieved by single-stage peak aging heat treatment (T6 treatment) for Al−Zn−Mg−(Cu) alloys. Nevertheless, the corrosion resistance of Al−Zn−Mg−Cu alloys following single-stage peak aging treatment is generally poor [6]. The continuous precipitates serve as corrosion channels along grain boundaries, expediting the corrosion process [3]. Researchers have developed various heat treatment processes to reconcile the conflicting attributes of high strength and corrosion resistance. After two-step over-aging treatment (T7x), the corrosion resistance of Al−Zn−Mg−Cu

Corresponding author: Sheng-ping WEN, Tel/Fax: +86-10-67396439, E-mail: wensp@bjut.edu.cn;
Zuo-ren NIE, Tel/Fax: +86-10-67391536, E-mail: zrnie@bjut.edu.cn
https://doi.org/10.1016/S1003-6326(25)66875-0

alloys demonstrates a noticeable improvement, but during the over-aging process, Al−Zn−Mg−Cu alloys experience a reduction in strength of approximately from 10% to 15% [7,8] as a result of the coarsening of precipitates inside the grain. The 10%−15% loss in strength is quite severe for Al−Zn−Mg−(Cu) series alloys, especially in the aerospace sector.

In order to minimize the strength degradation resulting from two-step over-aging (T7x), the retrogression and re-aging (RRA) heat treatment technique has been engineered [9], which led to the corrosion resistance of 7xxx series alloys in the T7x temper while strength levels maintaining at those under T6 condition. However, the RRA heat treatment includes a retrogression process carried out at approximately 170−280 °C and the time of the retrogression process is only several minutes (typically <10 min) [3]. So, the application of RRA heat treatments is primarily limited to thin section components, as it cannot achieve complete transformation and uniform performance in thick sections within short regression time. Finally, RRA heat treatment is not suitable for thick and large structural materials [10,11].

The microalloying technique is considered one of the most effective approaches to regulating precipitation evolution and improving properties of Al alloys [12−14]. The addition of Er promotes the formation of a large number of Al_3Er phases in the Al matrix [15], which greatly improves the mechanical properties of the Al alloy. However, the influence of Er on the corrosion resistance of Al alloys is often ignored, which is mentioned only in a few literatures [16]. Therefore, it is necessary to reveal the effect of Er on the corrosion resistance of Al alloys to understand the influence of Er microalloying.

Literatures [17,18] show that Si promotes the aging response and changes the evolution process of the precipitated phase. As a result, the strength of the Al alloy increases significantly. The co-addition of Si and Er is expected to regulate the evolution of the precipitated phase and further improve the comprehensive properties of Al alloys. In this work, we intend to improve the strength and corrosion resistance of Al−Zn−Mg−Cu alloys under single stage peak aging condition by co-microalloying with Si and Er.

If the evolution process of intergranular and grain boundary precipitates can be adjusted and controlled by microalloying under the condition of T6, the desired microstructures of high-strength and corrosion-resistant Al−Zn−Mg−Cu alloys are expected to be achieved. It is highly possible to overcome the deficiency of both T7x and RRA.

In present research, corrosion resistance and mechanical properties of the Al−Zn−Mg−Cu alloys containing Si and Er were investigated. The research results may provide some insights for the development of Al−Zn−Mg−Cu alloys with high strength and corrosion resistance under single-stage peak aging conditions.

2 Experimental

The experimental alloys were prepared using the traditional casting route. The master alloys (Al−50wt.%Cu, Al−27wt.%Si, Al−6wt.%Er) and high-purity aluminum, pure Zn, and pure Mg were used as raw materials to prepare experimental alloys. The raw materials were melted at 780 °C by using a VBF−1200X model air circulation resistance furnace, then melt was poured into an iron mold and 35 mm × 90 mm × 175 mm ingot was produced. The composition of experiment alloys was detected by X-ray fluorescence (XRF) spectroscopy. Element contents of experiment alloys are given in Table 1 and the experiment alloys are defined as Alloy 1 and Alloy 2 for convenience herein, respectively.

The ingots were subjected to a homogenization process (450 °C, 15 h). Subsequently, homogenized material was rolled into sheets (3 mm in thickness). The thickness of the material before hot rolling was machined to 15 mm. The deformation amount of

Table 1 Element contents of experimental alloys

Sample No.	Alloy	Actual composition/wt.%					
		Zn	Mg	Cu	Si	Er	Al
1	Al4.5Zn1.5Mg1.0Cu	4.48	1.51	1.10	0.03	−	Bal.
2	Al4.5Zn1.5Mg1.0Cu0.35Si0.1Er	4.49	1.53	1.04	0.38	0.12	Bal.

each pass was ~10%. The hot rolling process was carried out at 450 °C.

A solid solution heat treatment was conducted in following conditions: the samples were slowly heated from room temperature to 540 °C at a rate of ~2 °C/min and then kept at that temperature for 1 h, followed by immediate water cooling. To explore the optimal aging process under the single stage aging condition, the samples were further subjected to isothermal aging at 125, 175 and 225 °C for varying duration of 0.25, 0.5, 1, 3, 6, 12, 24, ⋯, 384 h, respectively.

The variations in hardness of the samples during the aging process were characterized using a hardness tester (model: Hxd-1000TM/lcd). The tensile test was performed using a universal testing machine (model: ETM−205D) to determine the ultimate tensile strength (abbreviated as UTS), yield strength (abbreviated as YS), and elongation (abbreviated as El) of the experiment alloys at their peak-aged state.

The IGC test was conducted in accordance with the ASTM G110—92 standard [19]. The pre-treated IGC samples were immersed in the test solution (57 g NaCl + 10 mL H_2O_2 (30%) + 1 L deionized water) for 6 h at (30±3) °C. The EXCO test was conducted in accordance with the ASTM G34—01 standard [20]. The pre-treated EXCO samples were immersed in the test solution (dissolving 234 g of NaCl and 50 g of KNO_3 in deionized water, adding 6.3 mL of concentrated HNO_3 (70 wt.%), and then diluting to 1 L) for 48 h at (25±3) °C. The optical microscopy technique (OLYMPUS PMG3 model) was utilized to observe the surface morphology and measure the maximum corrosion depths of the immersed samples. The cross-section of the immersed samples was selected for the analysis of the corrosion depth after being polished with metallographic sandpapers.

The electrochemical tests were carried out using a Bio-logic SP−150 three-electrode system. Polarization measurements were performed with an applied voltage range from −1.6 to 0.7 V and a scanning speed of 0.5 mV/s. A saturated calomel electrode (SCE) was worked as the reference electrode, a Pt electrode was used as the auxiliary electrode and 1 cm^2 of the alloy under investigation was used as the working electrode. A 3.5 wt.% NaCl solution was used as the test solution, which was kept at room temperature. In order to ensure the reliability of the results, repeated tests were conducted.

The metallographic microstructure of the experimental alloys was characterized using the OLYMPUS PMG3 optical microscope, and Keller solution (95 vol.% H_2O + 2.5 vol.% HNO_3 + 1.5 vol.% HCl + 1 vol.% HF) was used to etch polished specimen surfaces before samples were observed.

The microstructure analysis involved the utilization of a Titan G2 transmission electron microscope (TEM) operating at a voltage of 300 kV. For TEM observations, the samples with a diameter of 3 mm were carefully prepared using a twin-jet electro-polisher (model: MTP−1A). The electrolytic solution consisted of 25% HNO_3 and 75% CH_3OH. The twin-jet electro-polisher was operated at a current of 85 mA and a temperature of −25 °C approximately.

3 Results

3.1 Characterization of mechanical property

The aging hardening curve of the experimental alloys is shown in Fig. 1. The hardness value of Alloy 2 consistently exceeds that of Alloy 1 in the solid solution state, as depicted in Figs. 1(a−c). Alloys 1 and 2 exhibit similar isothermal aging hardening characteristics when aging at 125 °C. In 30 min, the hardness values of the two alloys experience a rapid increase, and then the hardness increases slowly until 384 h. When isothermal aging at 175 °C, the aging hardening responses of the two alloys are obviously different. Following a 30 min aging period at 175 °C, the aging hardening rate of Alloy 2 significantly exceeds that of Alloy 1, and Alloy 2 attains a much higher peak hardness (~HV 150) than Alloy 1 (~HV 110). The two alloys achieve their peak hardness more rapidly when subjected to isothermal aging at 225 °C, but the peak hardness is lower. In order to obtain higher hardness in a short time, 175 °C and 24 h are chosen as the optimal aging (peak-aged) condition for Alloy 2.

The tensile properties (UTS, YS and El) of two peak-aged alloys at 175 °C are given in Fig. 2. The UTS, YS, and El of Alloy 2 are 405.5 MPa, 339.5 MPa, and 14.0%, respectively, which are 29.0 MPa, 38.5 MPa and 4.5% higher than those of Alloy 1. The YS and El of Alloy 2 are significantly

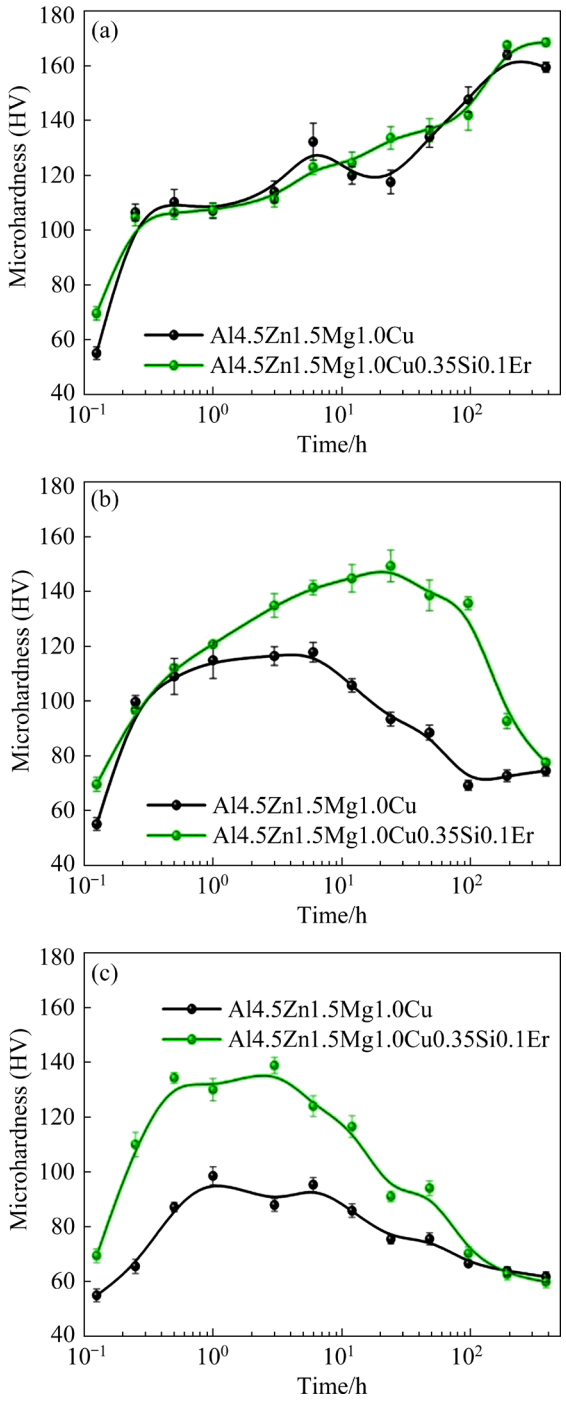

Fig. 1 Aging hardening curves of two alloys at 125 °C (a), 175 °C (b) and 225 °C (c)

enhanced due to the co-addition of Er and Si elements in the AlZnMgCu alloy.

Figure 3 shows experimental results after the IGC test. The surface morphology and the maximum corrosion depths of peak-aged alloys after immersion are displayed in Figs. 3(a−d). It is evident that there is scarcely corrosion occurring on the surface of Alloy 2, whereas Alloy 1 exhibits severe intergranular corrosion (IGC) characteristics on its surface. The maximum corrosion depth of Alloy 1 is 264.2 μm. However, in Alloy 2, the maximum corrosion depth is only 9.9 μm. After the addition of Er & Si, the maximum IGC depth decreases significantly from 264.2 to 9.9 μm. The IGC resistance of Alloy 2 is greatly improved. The addition of Er and Si elements can contribute to this phenomenon.

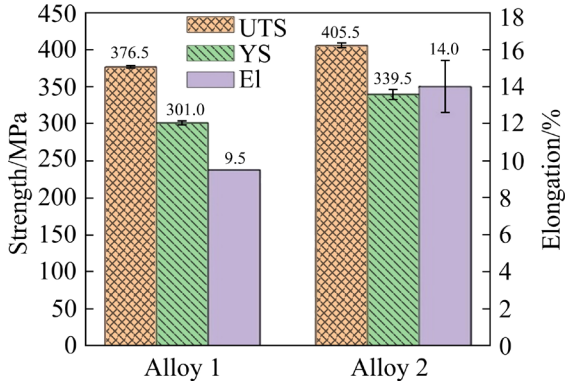

Fig. 2 UTS, YS, and El of two alloys at 175 °C under peak-aged conditions

Figure 4 exhibits experimental results after the EXCO test. The results show that the exfoliation corrosion sensitivity of Alloy 2 is up to the EA level compared to the EB level of Alloy 1. The synergistic effect of Er and Si elements significantly reduces the maximum depth of exfoliation corrosion (from 291.3 to 203.9 μm) and enhances the resistance to exfoliation corrosion.

The polarization curves of the two peak-aged samples immersed in 3.5 wt.% NaCl solution are displayed in Fig. 5. It can be seen that Alloy 2 exhibits a more negative corrosion potential ((−0.83±0.02) V) and a lower corrosion current density ((1.52±0.07) μA/cm^2), while Alloy 1 exhibits a more positive corrosion potential ((−0.80±0.02) V) and a higher corrosion current density ((2.97±0.11) μA/cm^2). According to the Faraday's law, the corrosion current density reflects the corrosion rate of the alloy, and the higher the corrosion current density, the faster the corrosion rate. Therefore, the corrosion resistance of Alloy 2 is better. According to the results achieved from the above experiment, the combined microalloying of Si and Er results in a synergistic enhancement of both mechanical properties and corrosion resistance in the peak-aged Alloy 2.

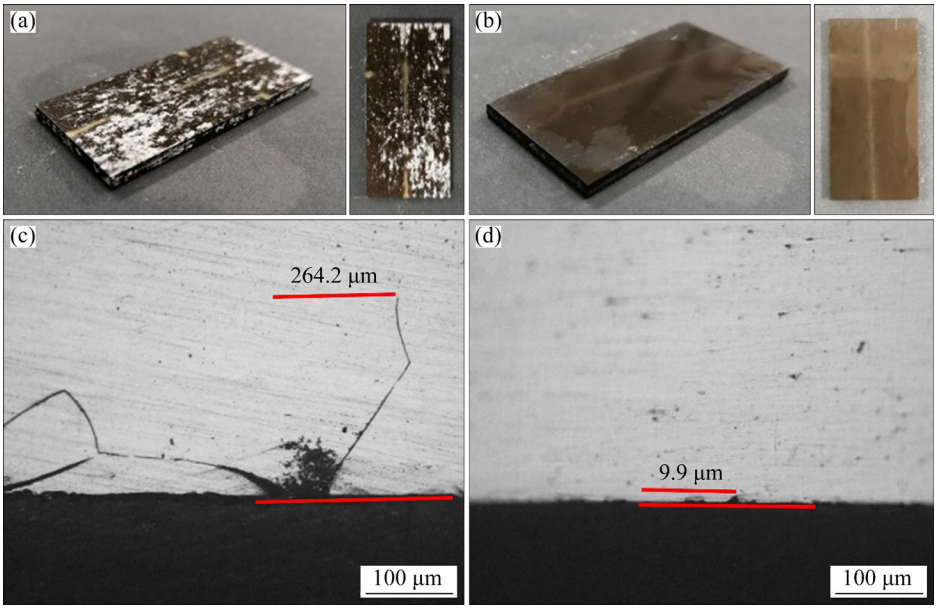

Fig. 3 Surface morphology (a, b) and maximum corrosion depths (c, d) of two alloys after IGC test: (a, c) Alloy 1; (b, d) Alloy 2

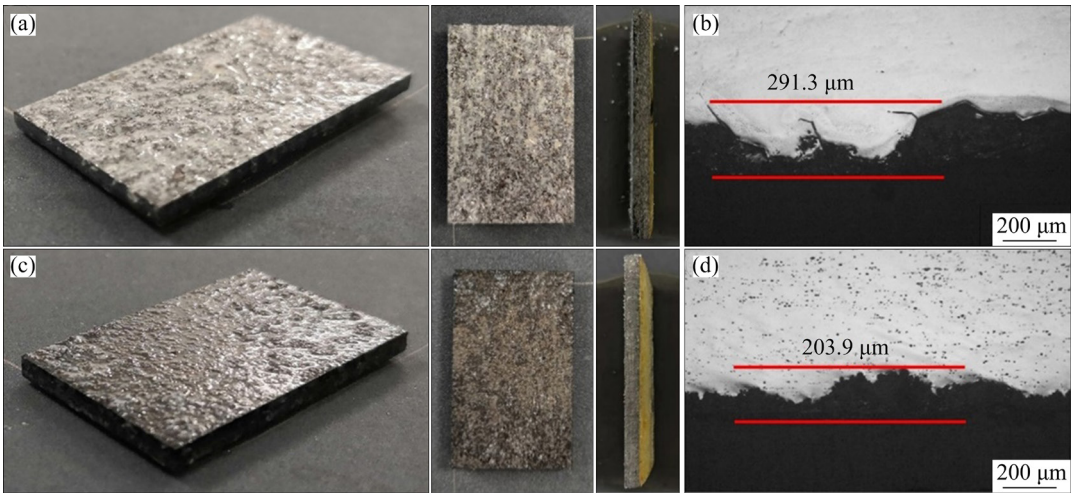

Fig. 4 Surface morphology (a, c) and maximum corrosion depth (b, d) of two alloys after exfoliation corrosion susceptibility test: (a, b) Alloy 1; (c, d) Alloy 2

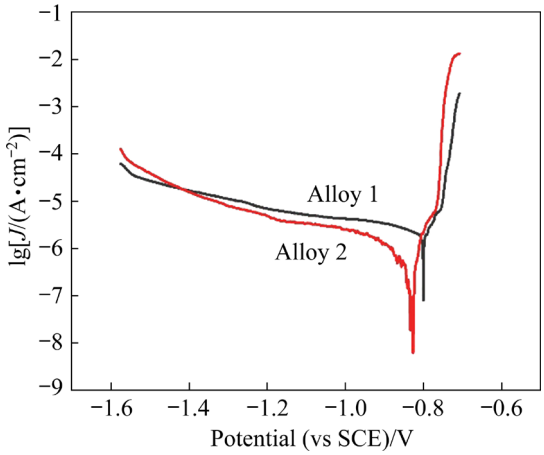

Fig. 5 Polarization curves of two peak-aged alloy immersed in 3.5 wt.% NaCl solution

3.2 Characterization of intragranular microstructure

Figure 6 demonstrates the intragranular microstructure of the two peak-aged alloys at 175 °C. Figure 6(a) illustrates that the predominant precipitated phase in Alloy 1 is the T' phase, with only a minimal presence of the η' phase. The corresponding selected area diffraction pattern (SADP) inserted in Fig. 6(a) provides further evidence of the abundant presence of the T' phase. Figure 6(b) displays two different morphologies of precipitates in Alloy 2, as confirmed by the SADP depicted in Fig. 6(c). The SADP verifies that these precipitates are composed of η' phases and GPB-II

zones [21]. It can be observed that the GPB-II zone exhibits a uniform distribution within the aluminum matrix. The presence of GPB-II zones contributes significantly to the boost in mechanical properties in Alloy 2.

3.3 Characterization of grain boundary microstructure

The corrosion resistance of age-hardening Al alloys is connected with the microstructure at the grain boundary. Figure 7 illustrates the microstructures of the grain boundaries of the two alloys at their peak-aged state at 175 °C. The grain boundary precipitated phase of Alloy 1 lies at the grain boundary in a continuous distribution, and the size of precipitation-free zone (PFZ) is about 200 nm, as shown in Fig. 7(a). On the grain boundary of Alloy 2, discontinuous precipitates are arranged along the grain boundary, and the average spacing between them is significantly increased compared to that of Alloy 1, as shown in Fig. 7(b). The local magnification in Fig. 7(c) reveals that the size of the PFZ in Alloy 2 is approximately 150 nm smaller than that of Alloy 1. This reduction is attributed to the formation of the GPB-II zone within the aluminum matrix. These results indicate that the co-microalloying of Er and Si regulates and controls the microstructure of grain boundaries, leading to the discontinuous distribution of precipitates along the grain boundary in Alloy 2. Several studies [22,23] have demonstrated that enhanced corrosion resistance of the AlZnMgCu alloy can be achieved through the discontinuous precipitates along grain boundaries because the continuous distribution of the grain boundary precipitates can often be used as a channel to induce corrosion.

Figure 8(a) illustrates the microstructure of Alloy 2 at grain boundaries before artificial aging. Figures 8(b−f) shows the corresponding element

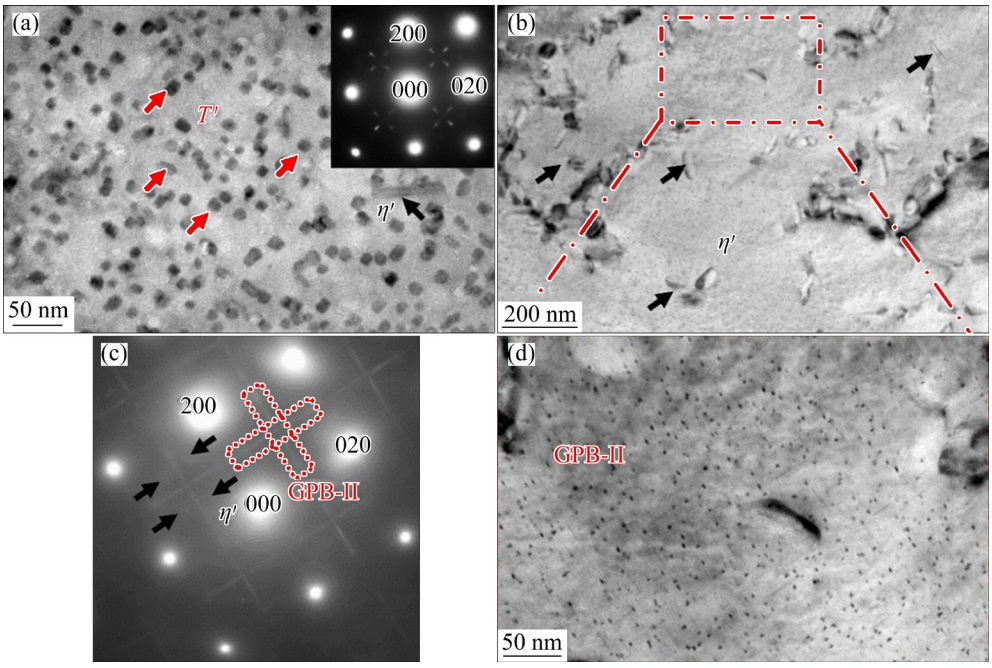

Fig. 6 Intragranular microstructures of peak-aged Alloys 1 (a) and 2 (b, d) at 175 °C; Corresponding SADP (c) of (b)

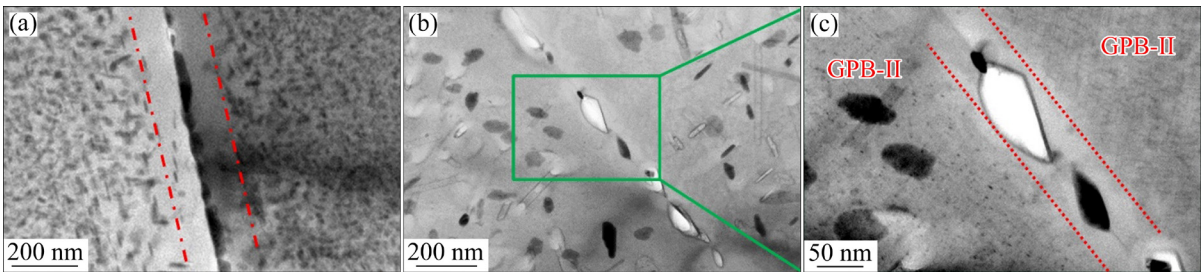

Fig. 7 Microstructures of grain boundaries in two peak-aged alloys at 175 °C: (a) Alloy 1; (b, c) Alloy 2

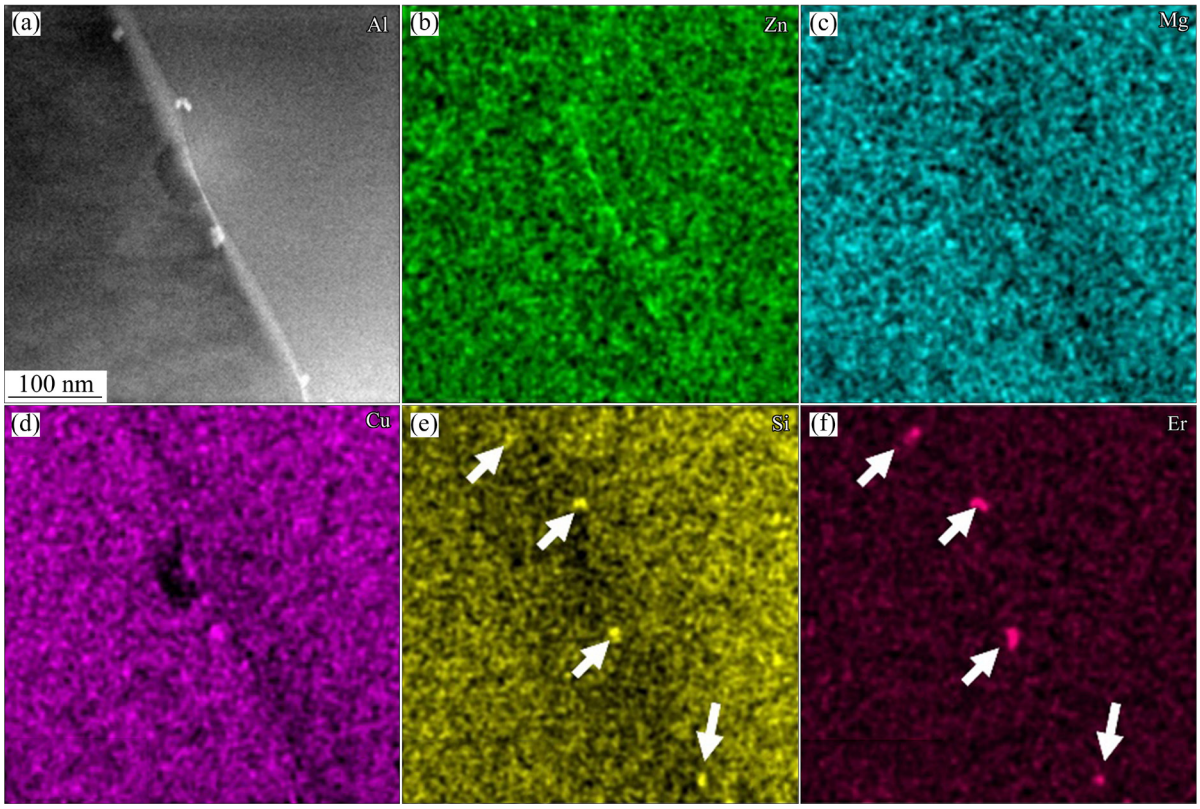

Fig. 8 Microstructure (a) and corresponding element mappings (b−f) at grain boundary of Alloy 2 before artificial aging (Mapping of Al is not shown here)

mappings at grain boundary (recorded in high-angle annular dark field (HAADF) mode). It can be seen from Figs. 8(e, f) that there are grain boundary precipitates rich in Er and Si elements on the grain boundaries (marked with white arrows), which contribute to the heterogeneous nucleation preferentially and precipitation of grain boundary η phase during aging. Therefore, grain boundary precipitates are coarser and more discrete in Alloy 2 compared with those in Alloy 1.

In addition, the metallographic images of the two alloys (solid-solution state) are shown in Fig. 9. There is a noticeable disparity in grain size between Alloy 2 and Alloy 1, with the former exhibiting a significantly smaller grain size. The pinning effect of Er−Si phases in Alloy 2 on grain boundaries makes it difficult for grain boundaries to migrate and merge, which leads to inhibiting grains growth and coarsening.

Figure 10 presents the metallographic images of the as-cast and as-homogenized alloys. The results show that the as-cast or as-homogenized grain size of Alloy 2 is just a little smaller than that of Alloy 1. This is mainly because the Er−Si phases may be formed during the hot-rolling process. The Er−Si phases have no contribution to the refinement of as-cast or as-homogenized grains. The small grain size of Alloy 2 is indeed affected by the tissue genetic effect of the initial grain size. However, the degree of influence of the pinning effect of the Er−Si phases is much greater than that of the tissue genetic effect.

The refined grain is also advantageous for enhancing the strength and elongation of Alloy 2. At the same time, according to reports from literatures [24,25], the corrosion resistance is also affected by the variation in grain size. Compared to the impact of grain size, the corrosion resistance of Alloy 2 is more prominently influenced by the distribution characteristics of grain boundary precipitates.

Figure 11 shows the elemental analysis of grain boundary precipitates in the peak-aged Alloy 2. The microstructure of Fig. 11(a) was recorded in HAADF mode. Element segregations at the grain boundary are not obvious, so the grain boundary contrast is not clear in this model. The observation in Fig. 11(b) clearly reveals that the concentration

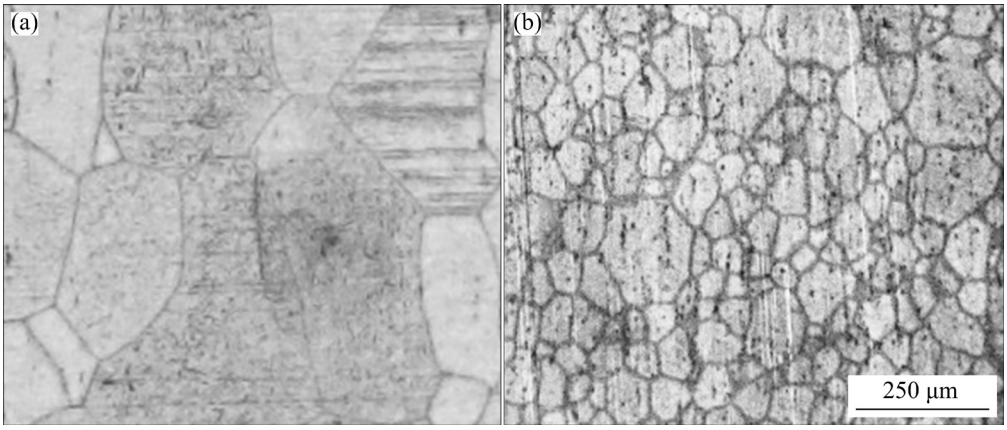

Fig. 9 Metallographic images (solid-solution state) of Alloy 1 (a) and Alloy 2 (b)

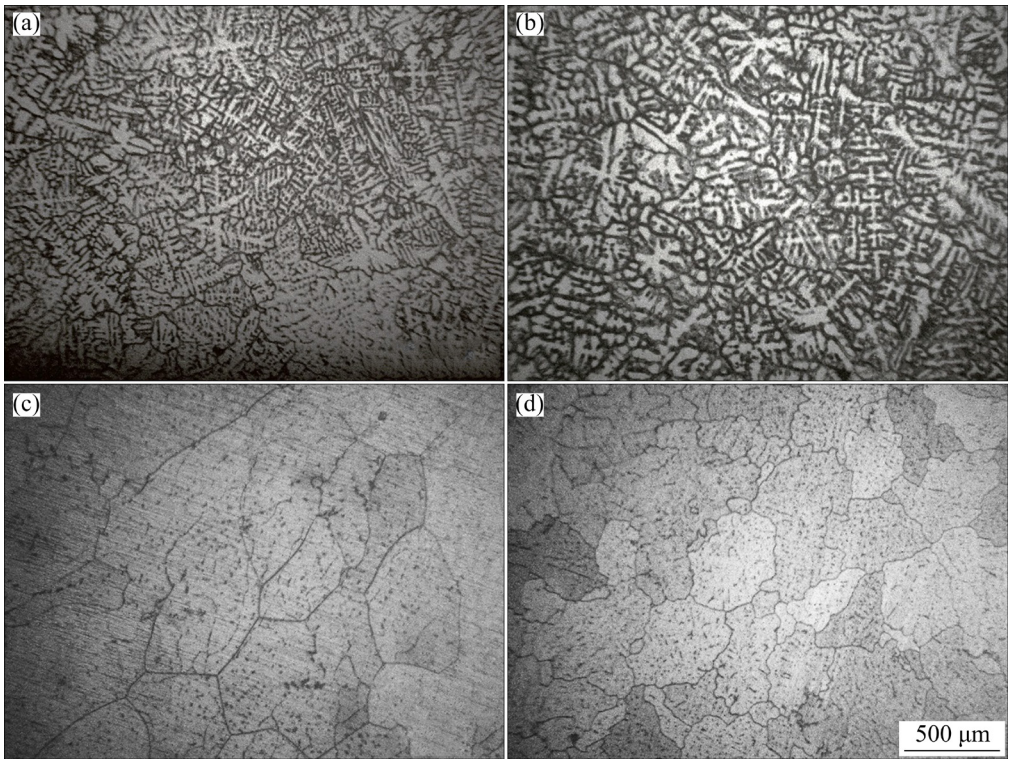

Fig. 10 Metallographic images of as-cast (a, b) and as-homogenized (c, d) alloys: (a, c) Alloy 1; (b, d) Alloy 2

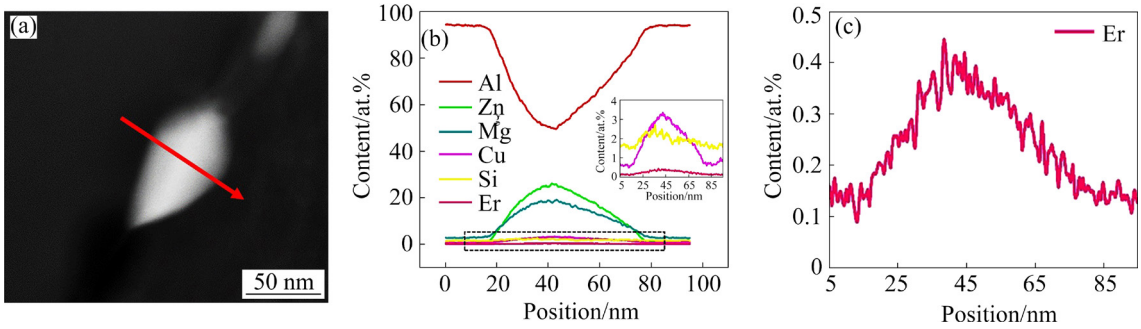

Fig. 11 Elemental analysis of precipitates along grain boundaries in peak-aged Alloy 2: (a) Grain boundary precipitates (recorded in HAADF mode); (b) Content of elements in grain boundary precipitates (along red arrow); (c) Local magnification (changes in Er content) of (b)

of Mg and Zn elements in the grain boundary precipitates is notably high. Mg and Zn elements are the components of grain boundary η phase. The inset (local magnification) in Fig. 11(b) reveals that the Cu element has an obvious segregation in the grain boundary precipitates. More importantly, Er and Si elements are detected in the grain boundary precipitates. Figure 11(c) clearly reflects the change of Er content. The content of Er is about 0.45 at.%, which is much higher than that in the matrix of Alloy 2. However, the precipitates along grain boundaries of the peak-aged Alloy 1 do not contain Er and Si elements (not shown here). These experimental results indicate that grain boundary precipitates of peak-aged Alloy 2 may rely on the Er−Si phases (as mentioned in Fig. 8) for nucleation and growth.

4 Discussion

4.1 Relationship between microstructure and mechanical properties

According to the experimental results in Fig. 1, Alloy 2 exhibits a higher hardness value compared to Alloy 1 under solid solution conditions. The co-addition of Si and Er elements results in a higher concentration of solute atoms in the matrix of Alloy 2 compared to that in the matrix of Alloy 1. Alloy 2 exhibits higher hardness values than Alloy 1 at the aging state (at 175 °C), primarily attributed to the formation of numerous small and dispersed GPB-II zones in the former (as illustrated in Figs. 6(b, d)). However, in Alloy 1, the predominant strengthening phase is the relatively large T' phase (see Fig. 6(a)). These results indicate that the precipitate evolution sequence of AlZnMgCu alloy is changed by the co-addition of Er and Si. The size of the T' phase (~15 nm) is significantly larger than that of the GPB-II zone (~5 nm).

The GPB-II zone is a metastable phase and its strengthening effect is more excellent than that of the T' phase, which has been confirmed in our latest work [21]. The GPB-II zone was first discovered and named in AlMgCu alloy containing 0.12% Si [26]. Subsequently, the GPB-II zone is found in AlZnMgCu alloy, but the GPB-II zone is observed only near the grain boundary, as reported in relevant literature [27]. In our present research, a large amount of GPB-II zone is discretized and evenly distributed in the Al matrix due to co-microalloying with Er and Si. The appearance of the GPB-II zone in the Al matrix greatly improves the mechanical properties of Alloy 2. The η' phase is widely recognized as the primary strengthening phase in AlZnMg(Cu) alloys [22]. The two-phase synergistic strengthening of η' phases and GPB-II zone is realized in Alloy 2. The excellent thermal stability of GPB-II zone ensures that the precipitates of Alloy 2 cannot be severely coarsened during peak aging treatment (at 175 °C or above). So, Alloy 2 demonstrates superior mechanical properties (strength and hardness) compared to Alloy 1.

Figure 2 also shows that Alloy 2 exhibits significantly higher elongation (14.0%) compared to Alloy 1 (9.5%), indicating that the microalloying of Si and Er elements significantly improves the elongation of the alloy. Further, Fig. 7(b) demonstrates that precipitated phases along grain boundaries in Alloy 2 are discontinuously distributed, while the precipitates along grain boundaries in Alloy 1 are continuously distributed. The continuous distribution of grain boundary precipitates is detrimental to the elongation of AlZnMgCu alloys, which weakens the binding force between adjacent grains. The synergistic effect of Si and Er elements changes the morphology and distribution characteristics of grain boundary precipitates of AlZnMgCu alloy. In detail, the microalloying of Si and Er elements leads to the formation of the grain boundary precipitates rich in Er and Si elements (see Fig. 8). The precipitates rich in Er and Si elements ultimately promote the formation of an interrupted distribution of the grain boundary phases in Alloy 2 (see Figs. 7(b, c)). At the same time, the reductions of PFZ width (from 200 to 50 nm) are proved in Alloy 2. In the precipitation-free zone, slip bands and stress concentrations are preferentially relieved, resulting in enhanced strength and elongation of the aluminum alloy [28,29]. The mechanical properties of AlZnMg(Cu) alloys are improved by a narrower width of the PFZ, which is positively correlated with elongation [29].

On the other hand, smaller grains also contribute to improving the strength and elongation of AlZnMgCu alloy. However, the characteristics of the grain boundary precipitates and the width of PFZ are the more important factors affecting the elongation compared to the size of the grain. Based on the above analyses, the co-addition of Er and Si

elements obviously improves the mechanical properties of AlZnMgCu alloys.

4.2 Relationship between evolution of precipitated phases and corrosion resistance

The experimental results in Figs. 3−5 and Fig. 7 show that the co-microalloying of Si and Er elements in Alloy 2 leads to a noteworthy enhancement in its corrosion resistance. The further reason is that Er and Si elements regulate and control the precipitation process of precipitates along the grain boundaries. The regulation and control of Er and Si elements on precipitates along the grain boundaries originates from the formation of nano-scaled Er−Si phases at grain boundaries (see Fig. 8), and grain boundary precipitates of peak-aged Alloy 2 rely on the Er−Si phases for nucleation and growth (see Fig. 11). Finally, co-addition of Er and Si affects the distribution characteristics of grain boundary precipitates during aging (see Fig. 7). So, in the peak-aged Alloy 2, the precipitates along the grain boundaries are discretely distributed.

There are two fundamental opinions regarding the corrosion mechanism of Al−Zn−Mg−(Cu) alloy. Firstly, the existence of potential differences between the precipitates situated at the grain boundaries and the adjacent electrodes leads to the anodic dissolution of the precipitates at the grain boundaries. The electrode potentials of the equilibrium η phase along the grain boundaries, PFZ, and Al matrix of aged AlZnMg(Cu) alloy are −0.86, −0.57, and −0.68 eV, respectively [3]. The corrosion potential (φ_{corr}) value of PFZ and Al matrix is positive to that of η phase at the grain boundary. The equilibrium η phase at the grain boundary is always anodic with respect to the Al matrix and its surrounding PFZ.

The continuous η precipitates on the grain boundaries are extremely susceptive anodic channels, which provide paths for the initiation and propagation of IGC in Alloy 1. The discontinuous and coarse grain boundary precipitates cut off the anode corrosion channel, and then reduce the corrosion rate of Alloy 2 to some extent. Literature research [30] has shown that the increasing content of intragranular precipitates may have the potential to enhance the IGC resistance by diminishing the potential difference between the grain and the PFZ. In present research, the volume fraction of the intragranular precipitates is obviously increased by the co-precipitation of the GPB-II zone and η' phases inside the grain, which may be an important reason for enhancing IGC resistance of Alloy 2 and more detailed reasons need to be further studied.

Secondly, the width of the PFZ is a crucial consideration affecting the susceptibility to IGC of AlZnMgCu alloys. Although the effect of PFZ on corrosion resistance is controversial, a large number of research results [31−33] show that the widened PFZ dramatically deteriorates the IGC resistance. In other words, as the width of PFZ narrows, the IGC resistance gradually increases. The PFZ size of Alloy 2 is much smaller than that of Alloy 1, and the IGC resistance of Alloy 2 is superior to that of Alloy 1.

In brief, the enhancement of the corrosion resistance can be attributed to the decrease in the size of the PFZ and the discontinuous distribution of grain boundary precipitates.

5 Conclusions

(1) The synergistic effect of Si and Er elements improves the strength and elongation of AlZnMgCu alloy. The yield strength experiences a significant enhancement of 38.5 MPa, accompanied by a notable increase in elongation of 4.5%.

(2) Improvement of mechanical properties is caused by the synergistic strengthening of the η' phases and the novel nano-scaled metastable GPB-II zone, especially the GPB-II zone.

(3) The corrosion resistance of AlZnMgCuSiEr alloy is greatly improved. The simultaneous addition of Si and Er elements facilitates the discrete dispersion of precipitates along the grain boundaries and leads to a substantial reduction in the width of the PFZ.

CRediT authorship contribution statement

Shang-shang LIANG: Conceptualization, Supervision, Funding acquisition, Data curation, Writing − Original draft, Writing − Review & editing; **Sheng-ping WEN:** Data curation, Methodology, Investigation, Writing − Review & editing; **Ke-hong GUO:** Resources, Methodology, Data curation; **Bao-sheng LIU:** Investigation, Data curation; **Yong HU:** Funding acquisition, Data curation; **Wu WEI:** Software, Visualization, Investigation, Data curation; **Xiao-lan WU:**

Software, Visualization, Data curation; **Hui HUANG:** Resources, Methodology, Data curation; **Kun-yuan GAO:** Software, Visualization, Data curation; **Xiang-yuan XIONG:** Software, Visualization; **Zuo-ren NIE:** Resources, Methodology, Funding acquisition, Data curation.

Declaration of competing interest

The authors declare that they have no known competing financial interests or personal relationships that could have appeared to influence the work reported in this paper.

Acknowledgments

This research was funded by the National Key Research and Development Program of China (Nos. 2021YFB3700902, 2021YFB3704204, and 2021YFB3704205), the Beijing Lab Project for Modern Transportation Metallic Materials and Processing Technology, China, the Jiangsu Key Laboratory for Clad Materials, China (No. BM2014006), the Doctor Funds of Taiyuan University of Science and Technology, China (No. 20222063), the Fundamental Research Program of Shanxi Province, China (No. 202303021212216), the Award Fund for Outstanding Doctors in Shanxi Province, China (No. 20232045), the Scientific and Technological Innovation Programs of Higher Education Institutions in Shanxi Province, China (Nos. 2022L289, and 2022L280), and the Special Project for Transformation of Scientific Achievements, China (No. 202204021301025). Thanks are given to Prof. Man-ling SUI and Dr. Yue-shuai WANG for their help and support in TEM microstructure characterization.

References

[1] YANG H F, HUANG R S, ZHANG Y L, ZHENG S J, LI M N, KOPPALA S, KEMACHEEVAKUL P, SANNAPANENI J. Effect of rolling deformation and passes on microstructure and mechanical properties of 7075 aluminum alloy [J]. Ceramics International, 2023, 49: 1165−1177.

[2] SUN P, YANG H F, HUANG R S, ZHANG Y L, ZHENG S J, LI M N, KOPPALA S. The effect of rolling temperature on the microstructure and properties of multi pass rolled 7A04 aluminum alloy [J]. Journal of Materials Research and Technology, 2023, 25: 3200−3211.

[3] HUANG L P, CHEN K H, LI S, SONG M. Influence of high-temperature pre-precipitation on local corrosion behaviors of Al−Zn−Mg alloy [J]. Scripta Materialia, 2007, 56: 305−308.

[4] FREIXES M L, PEGUET L, WARNER T, GAUL B. Nanoscale perspective on the stress-corrosion cracking behavior of a peak-aged 7XXX-Al alloy [J]. Corrosion Science, 2024, 229: 111904.

[5] MARLAUD T, DESCHAMPS A, BLEY F, LEFEBVRE W, BAROUX B. Influence of alloy composition and heat treatment on precipitate composition in Al−Zn−Mg−Cu alloys [J]. Acta Materialia, 2010, 58: 248−260.

[6] SU J X, ZHANG Z, CAO F H, ZHANG J Q, CAO C N. Intergranular corrosion and exfoliation corrosion of aluminum alloy [J]. Journal of the Chinese Society of Corrosion and Protection, 2005, 25: 187−192.

[7] WANG D, ZHANG W X, YI Y P, HUANG S Q, HE H L, ZHANG J J. Influence of retrogression temperature and time on microstructure, mechanical properties and corrosion behaviors of cryogenically-deformed 7A85 aluminum alloy [J]. Transactions of Nonferrous Metals Society of China, 2024, 34: 392−407.

[8] ZHANG T, HOU Y Z, QUE B H, TIAN Y X, CHEN L. Combining pre-rolling with retrogression and re-aging treatment to balance strength and corrosion resistance of 7A99 Al alloy [J]. Transactions of Nonferrous Metals Society of China, 2023, 33: 2913−2925.

[9] ZHANG Y L, YANG H F, HUANG R S, SUN P, ZHENG S J, LI M N, WANG X J, DU Q B. Investigation of microstructure and corrosion resistance of an Al−Zn−Mg−Cu alloy under various ageing conditions [J]. Corrosion Science, 2024, 227: 111719.

[10] FERRER C P, KOUL M G, CONNOLLY B J. Improvements in strength and stress corrosion cracking properties in aluminum alloy 7075 via low-temperature retrogression and re-aging heat treatments [J]. Corrosion, 2003, 59: 520−528.

[11] XIAO Y P, PAN Q L, LI W B, LIU X Y, HE Y B. Influence of retrogression and re-aging treatment on corrosion behavior of an Al−Zn−Mg−Cu alloy [J]. Materials & Design, 2011, 32: 2149−2156.

[12] DENG P, MO W F, OUYANG Z Q, LING K, LUO B H, BAI Z H. Microstructural evolution and corrosion mechanism of micro-alloyed 2024 (Zr, Sc, Ag) aluminum alloys [J]. Corrosion Science, 2023, 224: 111476.

[13] HUANG R S, YANG H F, SUN P, ZHENG S J, LI M J, DUAN Y H. Effects of Mg contents on microstructures and corrosion behaviors of homogenization Al−Zn−Mg−Cu alloys [J]. Corrosion Science, 2023, 223: 111461.

[14] WANG Y, CAO L F, WU X D, LIN X M, Yao T Y, PENG L M. Multi-alloying effect of Ti, Mn, Cr, Zr, Er on the cast Al−Zn−Mg−Cu alloys [J]. Materials Characterization, 2023, 201: 112984.

[15] WU H, WEN S P, HUANG H, LI B L, WU X L, GAO K Y, WANG W, NIE Z R. Effects of homogenization on precipitation of Al_3(Er,Zr) particles and recrystallization behavior in a new type Al−Zn−Mg−Er−Zr alloy [J]. Materials Science and Engineering A, 2017, 689: 313−322.

[16] ZHONG H, LI S C, WU J L, DENG H L, CHEN J Q, YAN N, CHEN Z X, DUAN L B. Effects of retrogression and re-aging treatment on precipitation behavior, mechanical and corrosion properties of a Zr+Er modified Al−Zn−Mg−Cu alloy [J]. Materials Characterization, 2022, 183: 111617.

[17] LIANG S S, WEN S P, LIU Q X, WU X L, GAO K Y, HUANG H, NIE Z R. Effect of Si and Er on aging precipitation behavior of Al−Zr alloys [J]. The Chinese Journal of Nonferrous Metals, 2022, 32: 619−629. (in

Chinese)
[18] LIANG S S, WEN S P, WU X L, GAO K Y, HUANG H, NIE Z R. The synergetic effect of Si and Sc on the thermal stability of the precipitates in AlCuMg alloy [J]. Materials Science and Engineering A, 2020, 783: 139319.
[19] ASTM Standard G110—92. Standard practice for evaluating intergranular corrosion resistance of heat treatable aluminum alloys by immersion in sodium chloride + hydrogen peroxide solution [S]. 2015.
[20] ASTM Standard G34 — 01. Standard test method for exfoliation corrosion susceptibility in 2XXX and 7XXX series aluminum alloys [S]. 2013.
[21] GUO K H, LIANG S S, WEN S P, WEI W, HU J C, WU X L, GAO K Y, HUANG H, NIE Z R. GPB-II zone in Si microalloyed Al−Zn−Mg−Cu alloy and its strengthening effect [J]. Materials Science and Engineering A, 2022, 852: 143721.
[22] YANG L, GAO Q, TAO X C, HU B, CHEN L J. Effect of heat treatment on intergranular corrosion behavior of Al−6Zn−2Mg−2Cu alloy [J]. Transactions of Materials and Heat Treatment, 2016, 37: 62−66. (in Chinese)
[23] SU R M, QU Y D, YOU J H. Effect of pre-aging on stress corrosion cracking of spray-formed 7075 alloy in retrogression and re-aging [J]. Journal of Materials Engineering and Performance, 2015, 24: 4328−4332.
[24] GOLLAPUDI S. Grain size distribution effects on the corrosion behavior of materials [J]. Corrosion Science, 2012, 62: 90−94.
[25] ZHAO J H, DENG Y L, TANG J G, ZHANG J. Effect of gradient grain structures on corrosion resistance of extruded Al−Zn−Mg−Cu alloy [J]. Journal of Alloys and Compounds, 2020, 832: 154911.
[26] KOVARIK L, GOUMA P I, KISIELOWSKI C, COURT S A, MILLS M J. A HRTEM study of metastable phase formation in Al−Mg−Cu alloys during artificial aging [J]. Acta Materialia, 2004, 52: 2509−2520.
[27] MATSUDA K, YASUMOTO T, BENDO A, TSUCHIYA T, LEE S, NISHIMURA K, NUNOMURA N, MARIOARA C D, LEVIK A, HOLMESTAD R, TODA H, YAMAGUCHI M, IKEDA K I, HOMMA T, IKENO S. Effect of copper addition on precipitation behavior near grain boundary in Al−Zn−Mg alloy [J]. Materials Transactions, 2019, 60: 1688−1696.
[28] OGURA T, HIROSE A, SATO T. Effect of PFZ and grain boundary precipitate on mechanical properties and fracture morphologies in Al−Zn−Mg−(Ag) alloys [J]. Materials Science Forum, 2010, 638−642: 297−302.
[29] OGURA T, HIROSAWA S, CEREZO A, SATO T. Quantitative correlation between strength, ductility and precipitate microstructures with PFZ in Al−Zn−Mg(−Ag,Cu) alloys [J]. Materials Science Forum, 2006, 519: 431−436.
[30] CAO C, ZHANG D, WANG X, MA Q B, ZHUANG L Z, ZHANG J S. Effects of Cu addition on the precipitation hardening response and intergranular corrosion of Al−5.2Mg−2.0Zn (wt.%) alloy [J]. Materials Characterization, 2016, 122: 177−182.
[31] CHENG Q S, YE L Y, HUANG Q M, DONG Y, LIU S D. Effect of two-stage overaging on microstructure and corrosion properties of an Al−Zn−Mg−Cu alloy [J]. Journal of Materials Research and Technology, 2020, 20: 3185−3194.
[32] ZHAN X, TANG J G, LI H Z, LIANG X P, LU Y F, CHE Y X, TU W B, ZHANG Y D. Effects of non-isothermal aging on mechanical properties, corrosion behavior and microstructures of Al−Cu−Mg−Si alloy [J]. Journal of Alloys and Compounds, 2020, 819: 152960.
[33] LIU X Y, LI M J, GAO F, LIANG S X, ZHANG X L, CUI H X. Effects of aging treatment on the intergranular corrosion behavior of Al−Cu−Mg−Ag alloy [J]. Journal of Alloys and Compounds, 2015, 639: 263−267.

Er 和 Si 元素对峰时效态 AlZnMgCu 合金耐蚀性能的协同作用

梁上上[1,2]，文胜平[2]，郭科宏[2]，刘宝胜[1]，胡 勇[1]，魏 午[2]，
吴晓蓝[2]，黄 晖[2]，高坤元[2]，熊湘沅[2]，聂祚仁[2]

1. 太原科技大学 材料科学与工程学院，太原 030024；
2. 北京工业大学 材料科学与工程学院，北京 100124

摘 要：通过硬度测试、拉伸测试、晶间腐蚀测试、剥落腐蚀测试、透射电镜等手段研究了含 Si 和 Er 元素的峰时效态 AlZnMgCu 合金的耐蚀性能与力学性能。结果表明，η'相和纳米级 GPB-II 区可协同强化峰时效态 AlZnMgCuSiEr 合金。AlZnMgCu 合金的屈服强度提高 38.5 MPa，伸长率提高 4.5%。同时，Er 和 Si 元素的协同作用提高 AlZnMgCu 合金的耐蚀性能，最大晶间腐蚀深度从 264.2 μm 减小至 9.9 μm，其根本原因是 Er 和 Si 元素的复合添加可调控 AlZnMgCu 合金的晶内和晶界析出相的演变过程。

关键词：AlZnMgCu 合金；GPB-II 区；晶间腐蚀；剥落腐蚀；力学性能

(Edited by Bing YANG)